



Structurally restricted phase transitions in VO₂(B) and their impact on transport properties

Srinivasa Rao Popuri Popuri, Alla Artemenko, Rodolphe Decourt, Michaël Josse, U-Chan Chung Seu, Dominique Michau, Mario Maglione, Antoine Villesuzanne, Michaël Pollet

► To cite this version:

Srinivasa Rao Popuri Popuri, Alla Artemenko, Rodolphe Decourt, Michaël Josse, U-Chan Chung Seu, et al.. Structurally restricted phase transitions in VO₂(B) and their impact on transport properties. Journal of Physical Chemistry C, 2015, 119 (44), pp.25085-25092. 10.1021/acs.jpcc.5b07826 . hal-01225684

HAL Id: hal-01225684

<https://hal.science/hal-01225684>

Submitted on 27 Jan 2021

HAL is a multi-disciplinary open access archive for the deposit and dissemination of scientific research documents, whether they are published or not. The documents may come from teaching and research institutions in France or abroad, or from public or private research centers.

L'archive ouverte pluridisciplinaire **HAL**, est destinée au dépôt et à la diffusion de documents scientifiques de niveau recherche, publiés ou non, émanant des établissements d'enseignement et de recherche français ou étrangers, des laboratoires publics ou privés.

Structurally Restricted Phase Transitions in VO₂(B) and Their Impact on Transport Properties

S. R. Popuri^{†‡§}, A. Artemenko^{†‡}, R. Decourt^{†‡}, M. Josse^{†‡}, U. C. Chung^{†‡}, D. Michau^{†‡}, M. Miclau[§], M. Maglione^{†‡}, A. Villesuzanne^{†‡⊥} and M. Pollet^{†‡}*

[†]CNRS, ICMCB, UPR 9048, F-33600 Pessac, France

[‡] Univ. Bordeaux, ICMCB, UPR 9048, F-33600 Pessac, France

[§] INCEMC, Plautius Andronescu 1, 300224, Timisoara, Romania

[⊥] IREET, University of Bolton, Bolton, BL3 5AB, United Kingdom

*Corresponding author: pollet@icmcb-bordeaux.cnrs.fr

We have overcome the challenge associated with the low irreversible phase transition temperature of VO₂ (B) by using spark plasma sintering to obtain samples appropriate for reliable transport property measurements. All our data, transport, magnetic and thermal, converge in favor of a multiphasic system in which a low temperature phase (insulating and magnetically ordered), an intermediate temperature phase (insulating), and a high temperature phase (presumably metallic with strong electron correlations), coexist. The coexistence domain for the three phases is broad and extends over *ca* 60 K around 235 K. The low temperature phase is always associated to, at least, another phase and becomes dominant below 200 K. The high temperature phase is present over the full temperature range and exists alone above room temperature.

Keywords: VO₂, Structure-property relationships, Phase transitions, Metal-insulator transitions, Electron correlations

1. Introduction

Vanadium oxides display an exceptionally rich variety of structures with vanadium ions in different oxidation states ($3d^0$, $3d^1$, $3d^2$, and even $3d^3$).¹ They often exhibit a complex interplay between charge, spin, and orbital degrees of freedom that generally induces strong correlations, leading to remarkable electric and magnetic properties. This is particularly obvious in the case of the several VO_2 polytypes² that display more or less sharp change in their electronic behavior with temperature. VO_2 (R/M1) in particular received considerable attention over the last few decades because of its bistable switching near room temperature (RT) between an insulating state (low temperature (LT) monoclinic M1 phase with dimerized vanadium pairs and alternating V-V distances of 2.65 and 3.12 Å) and a metallic state (high temperature (HT) tetragonal R rutile phase with uniform V-V distances of 2.85 Å).³ At the metal-insulator transition (MIT), the resistivity varies over several orders of magnitude, which is likely to lead to important technological applications;⁴ in addition, the specifically fast switching of this system makes it a potential candidate for diverse optical as well as electrical switching applications.^{5,6} The metastable VO_2 (B) polymorph was also proposed to exhibit such structural transition and a MIT near RT.^{7,8} From the crystal structure perspective, VO_2 (B) is quite different from VO_2 (R/M1) although some similarities can be observed: while VO_2 (R/M1) shows an interconnection (via corner sharing VO_6 octahedra) of 1D linear and packed substructures (edge sharing VO_6 octahedra) conducive to pure σ bonding and to a Peierls state at LT, VO_2 (B) is a stack (also via corner sharing VO_6 octahedra) of more complex and diffuse 2D blocks (also based on edge sharing VO_6 octahedra). The unit cell is monoclinic (C2/m; Z=4) and contains two vanadium sites labeled V1 and V2 in close distorted octahedral coordination; both cations are off-centered what results in a low local symmetry (C_s in Schoenflies notation) and very different metal-oxygen and metal-metal distances, as shown in Fig. 1. In each block, VO_6 octahedra share edges either in (ac) plan for V2 cations (short green bonds at 2.896 Å in Fig. 1, *i.e.* less than 2% longer than the V-V bond in VO_2 (R) (2.85 Å)³) or in (bc) plan for V1 cations with zigzag chains along [010] (long red bonds -3.331 Å-); whenever V1 and V2 share their oxygen environment, the sharing is either in (ac) plan (long orange bonds -3.239 Å-) or in (ab) plan with zigzag chains along [010] (medium blue bonds -3.058 Å-); in addition, oxygen octahedra around V2 are share corners in the [010] direction.

VO₂ (B) polymorph was significantly investigated as an electrode material in rechargeable aqueous lithium ion batteries, due to its promising electrochemical properties, but inconsistent reports were given in terms of magnetic properties.^{9,10,11} In addition, although it was discovered nearly four decades ago, studies on its electrical transport properties are limited to some observations of its semiconducting behavior from current-voltage characteristics and resistivity measurements performed on pressed pellets and drops of suspension dried on a wafer.^{8,12,13} Indeed, a major challenge for accessing its intrinsic transport properties is associated with its irreversible transformation into the VO₂ (R) polymorph at 500°C, which hinders the sintering and prevents from a sufficient consolidation of the material.² In this article we present the electronic transport properties of VO₂ (B) pellets consolidated using spark plasma sintering (SPS); we also revisit its magnetic properties that we finally correlate with its structural properties, based on the present knowledge of the VO₂ (R/M1) system.

2. Experimental details

Plate-like VO₂ (B) particles with average coherence length *ca.* 65 nm were prepared at 493 K for 2 hr using a hydrothermal process from precursors V₂O₅ and citric acid. For preparation of polycrystalline VO₂ (M1), appropriate stoichiometric amounts of high-purity V₂O₃ and V₂O₅ were sealed in evacuated quartz tube and slowly heated to 750 °C and then held there for 48 h. X-ray Powder diffraction (XRPD) patterns were recorded using a PANalytical X'Pert PRO MPD diffractometer with Cu K_{α1} radiation and analyzed by Rietveld method using the FullProf suite.¹⁴ The morphology of the products was examined by a field emission scanning electron microscope (FESEM, JEOL JSM-6300F, 15kV): energy dispersive X-ray spectroscopy (EDX) coupled to the FESEM was used to check for the chemical content and the homogeneity of the products. Electron paramagnetic resonance (EPR) experiments were performed at 9.4 GHz with a standard 3 cm wavelength Bruker spectrometer; an Oxford Instrument ESR 900 cryosystem allowed operating at temperatures from 4 to 300 K. The powder samples were densified using SPS technique (SINTER® LAB Series; SPS-511S); the powder was loaded into a carbon die and heated up to 523 K with a heating rate of 100 K/min under a pressure of 90 MPa; after dwelling 5 min, the pressure was released and the sample was cooled down to RT. Before proceeding to the transport characterizations, the quality of the pellets after the SPS treatment was thoroughly checked. The electric dc resistivity - four-probe method - and the Seebeck coefficient were measured in the 4-300 K range with

homemade equipment.¹⁵ Capacitance and dielectric losses were measured as a function of temperature from RT down to 10 K, using a HP4194A impedance bridge in the frequency range 1 kHz–1 MHz, using a homemade sample holder in a Quantum Design physical properties measurement system (PPMS®).¹⁶ The measurements of magnetic properties and specific heat were carried out on powder samples using Quantum Design magnetic property measurement system (MPMS®) and PPMS®, respectively.

3. Results

The overall quality of the VO₂ (B) powder samples was checked using XRPD experiments as well as infrared spectroscopy studies (not shown) to discard from any hydration of the samples.² The RT profile refinements agree with previous reports with an indexation matching space group C2/m and cell parameters $a=12.0417$ (3) Å, $b=3.6892$ (8) Å, $c=6.4312$ (2) Å and $\beta=106.965$ (2)°; no extra peaks or peak splitting could be detected (Figure 2a).² After the SPS treatment, the final density of the pellet is *ca.* 80%; the transport properties reported hereafter can thus be tarnished with the low density of the pellet; however, we believe that the observed global trends account for some reliable intrinsic features of the compound. Surface XRPD measurements carried out on the pellets confirmed the presence of VO₂ (B) only (Figure 2a). SEM images of powders before SPS and the cross-sectional view of a SPS-elaborated pellet are shown in Figs. 2a and 2b, respectively. They account for the densification of the sample and the retention of the plate-like morphology of the particles after sintering.

The macroscopic magnetic measurements results are shown in Fig. 3; several distinct regimes are displayed, as already reported.⁷ As compared to previous reports however, our results (recorded at low speed in settle mode at about 10 K/hr), clearly evidence a second soft maximum at *ca* 230 K (hollow in the insert showing 1/M) leading globally to a soft regime between 220 K and 280 K, where the magnetization magnitude barely changes. The existence of these several regimes is related to the coexistence -over a large temperature domain far beyond the mean transition temperature- of several phases, as shown by Oka et al.⁷ with paramagnetic vanadium ions in a HT phase and the formation of non-magnetic V-V pairs (spin singlets) in a LT phase; furthermore, at lower temperatures, the magnetic susceptibility seems to saturate what could be ascribed to the ordering of some free spins. Our results also reflect the progressive nature of the structural transition which gradually occurs over a wide temperature range. Similar observations were made in the case of the VO₂ (A) polymorph,

signing the different nature or origin of the transition in these polymorphs as compared to VO₂ (M1), which displays a quite sharp transition.¹⁷

Both the low (25-200 K) and high (320-350 K) temperature regions of the magnetic susceptibility can be modeled with a Curie–Weiss law and a temperature independent term, *i.e.* $\chi(T) = \chi_0 + C/(T + \theta)$. Using the phase proportion p_{LT} reported by Oka et al.⁷ for the LT phase (bottom panel in Fig. 2; $p_{LT}^{max} = 0.69$ as reported), we can propose a model to the magnetization as $\chi(T) = p_{LT}[\chi_0^{LT} + C^{LT}/(T + \theta^{LT})] + (1 - p_{LT})[\chi_0^{HT} + C^{HT}/(T + \theta^{HT})]$ (values given in Table 1); this model is plotted as a green dashed line in Fig. 3. As expected, it matches with both the LT and HT data (from 25 K to 200 K and from 280 K to 350 K, respectively) but the intermediate temperature (IT) region is not accounted for. The Curie constant for the HT phase matches with 100% free spin for the V⁴⁺ 3d¹ cation; the interactions are antiferromagnetic as expected from unpaired vanadium cations; the constant term is purely diamagnetic and close to the value determined from the contributions of the atomic cores (-30×10^{-6} emu/mole). At LT, the Curie constant decreases dramatically and represents only 12% of the contribution expected from a V⁴⁺ 3d¹ cation (*i.e.* a value coinciding with the contribution of only one cation over the eight present in the unit cell); the interactions are weakly ferromagnetic in agreement with the observation of the magnetization saturation at very LT; the order of magnitude of the temperature independent term is consistent with the values reported for VO₂ (M1) ($\chi_0 \sim 100 \times 10^{-6}$ emu/mole) and VO₂ (M2) ($\chi_0 \sim 200 \times 10^{-6}$ emu/mole).¹⁸

The difference between the full data set and this simple model actually shows an asymmetric peak in the magnetization, centered at *ca* 225 K and of width at half maximum of about 30 K. This excess magnetization can be accounted for, assuming the transient presence of an intermediate phase obeying a simple Curie law (see the bottom panel in Fig. 3 with a Gaussian peak centered at 233 K and a standard deviation of 14 K). The temperature domain involved is small what makes the correlation between the Curie constant and the phase proportion quite important. We could obtain a good fit to the data with a maximum proportion of this phase at *ca* 12% and $C=0.1875$; this latter value corresponds to 50% of the contribution expected from a V⁴⁺ 3d¹ cation, *i.e.* the contribution of half the cations in the unit cell. Keeping in mind that V2-V2 distances are quite short (2.895 Å) at HT (almost like in VO₂ (R)) while all others exceed 3 Å, such result sounds reasonable and can be explained with

an intermediate regime where only V2 cations strongly interact to form spin singlets while leaving free the electron spins on V1 cations. As the temperature decreases, the proportion of the intermediate phase decreases as it feeds the LT phase. We further note the presence of a small hysteresis between FC and ZFC regimes in the IT region; this indicates the probable presence of antiferromagnetic interactions and the ordering between V1 electrons (long zigzag chains in about (bc) plan; red bonds in Fig. 1) and/or V1 and V2 electrons (shorter zigzag chains in (ab) plan; blue bonds in Fig. 1) which results in the observed decrease of the Curie constant in the LT phase.

Results of X-band EPR measurements carried out on the powder sample across the transition from 180 K to RT are shown in Fig. 4. All spectra below RT consist of a very weak hyperfine structure superimposed on a broad resonance line. The set of hyperfine lines comes from isolated V^{4+} ions and is due to the dipole–dipole interaction between the nucleus magnetic moment (nuclear spin for ^{51}V isotope $I = 7/2$) and the unpaired electron moment ($S = 1/2$ for a V^{4+} ion). It is present on the full temperature range below RT and accounts for the presence of localized carriers in the sample. The broad resonance line is more likely due to spin–spin exchange interactions and can result from interacting V-V pairs as well as interacting electrons on isolated V cations. Its intensity barely changes between about 230 and 280 K but it increases below *ca* 230 K and fast drops above 280 K; this observation agrees with the macroscopic magnetic measurements discussed above and suggests a strong weakening of the interactions at HT and a two-steps setting up below RT with, first, short range interactions down to 230 K and then a final bolting with the onset of longer range interactions. The absence of signal at RT may indicate the presence of delocalized charges only.

Heat capacity measurements recorded with and without applied magnetic field are shown in Fig. 5, as well as the difference curve. No clear anomaly marking a transition could be seen from the data sets. Satisfactory global fits to the data (for the whole temperature range) could be obtained assuming two Debye contributions, a Sommerfeld term and a small Schottky contribution (about 10% of the HT phase contribution; *(see below)* probably resulting from the crystal field splitting of the ground state level (3 and 2 non degenerated levels at 0 and 9 T, respectively); in both cases, the oscillators sum was constrained at 3, *i.e.* the number of atoms per formula unit. The fit at 0 T shows a clear deviation from the data at *ca* 235 K while the fit at 9 T follows the data set on the full temperature range. In both cases, the respective proportions of oscillators are about 0.25/0.75 for the first and the second Debye contribution.

These values are, in essence, quite close to the proportions 0.31/0.69 reported by Oka⁷ and used to fit our magnetic data (*see above*). However, all our attempts to fit the heat capacity data using the same kind of model, *i.e.* taking into account the proportions of the different phases, failed; this can be related to both the slow rate of the measurements and the non-constant conditions during the data acquisition (uneven relaxation time) that affects the dynamic of the system; in addition, the use of a secondary vacuum during the experiment can shift the overall LT to HT phase transition to higher temperatures and modify the phase ratio. Assuming that the proportion of oscillators relates to the different phases, the Debye temperature (θ_D) for the LT phase is 850 K and is independent on the magnetic field, while it is much lower for the HT phase ($\theta_D=335$ K without applied magnetic field) and is slightly dependent on the magnetic field (-21 K with 9 T). Such a decrease of the θ_D across the transition is in agreement with the available results on the rutile polymorph with *ca* 650 K at LT (VO_2 (M1)) and *ca* 450 K at HT (VO_2 (R)) determined from thermal displacements observed in X-ray measurements.¹⁹ It is also in agreement with the classical view of a lower θ_D for more metallic structures, what can indeed be expected for the HT phase in an electrons delocalized picture in the MIT assumption; to this extend, it also highlights a strong localization of the carriers as the temperature decreases; The calculated Sommerfeld coefficients are *ca* 7 and 19 mJ/mol.K² without and with magnetic field respectively. Keeping the LT electrons localized picture ($\gamma \rightarrow 0$), one should assume that it entirely arises from the HT phase which represents about one fourth of the LT contribution to the heat capacity; in other words, after rescaling to the HT phase proportion, the Sommerfeld coefficient actually reaches *ca* 27 and 79 mJ/mol.K² without and with magnetic field respectively, indicating both quite strong electron correlations in the HT phase and a non-negligible effect of the magnetic field.

The difference curve in Fig. 5 is quite noisy as it includes the noise of both the high and zero magnetic field data; however, two distinct regimes are visible below and above 233 K. In addition to this, several other anomalies are also visible at lower temperature such as *ca* 77 K and 200 K. However, it becomes very speculative to discuss them as the signal to noise ratio increases when the temperature decreases; the biggest anomaly at *ca* 77 K could for instance be related to nitrogen condensation. Both regimes globally follow a linear trend. At LT, the slope is about 11 mJ/mol.K², *i.e.* roughly the difference in the Sommerfeld coefficients discussed above. At HT, above 233 K (when the fit at 0 T departs from the data), the slope is

about 81 mJ/mol.K² and denotes strong interactions. Following the discussion above, it sounds reasonable to propose that this temperature domain coincides with the region when an intermediate phase exists with only interacting V2 pairs but strong spin interactions between other vanadium electrons; the temperature for the crossover, 233 K, actually remarkably matches with the center of the distribution used to fit the magnetic data in the intermediate region; in addition, the anomaly at 200 K coincides with both the first decrease in LT phase and the increase of the HT phase as well as the appearance of the first significant traces of intermediate phase (bottom panel in Fig. 3).

DC transport properties are shown in Fig. 6; data only down to 80 K for the electrical resistivity and 120 K for the Seebeck coefficient are available because the samples become too resistive at lower temperature. The resistivity decreases with increasing temperature evidencing a semiconducting behavior; at 290 K, $\rho=45 \text{ } \Omega\cdot\text{cm}$ is about 5 times lower than previously reported values on compacted powders.⁸ No clear anomaly is directly visible on the raw data sets. The resistivity data can be modeled using Mott's law²⁰ $\sigma = \sigma_0 \exp[-(T_0/T)^{1/n}]$ where $k_B T_0 = \frac{4}{3}\pi W \cdot \left(\frac{R}{\zeta}\right)^3$ with W the hopping energy, R the hopping distance, ζ the localization length and where σ_0 depends on the phonon spectrum and scales as phonon frequency ν_{phonon} . The refined values are $T_0 = 2.42 \times 10^6 \text{ K}$ and $\sigma_0 = 1.44 \times 10^7 \text{ S}\cdot\text{cm}^{-1}$ using the exponent $n=3$. This suggests a strong localization picture and conduction *via* a variable range hopping mechanism. The exponent in Mott's law is often used as a criterion for the dimensionality of the mechanism. Here, the quality of the fits (not shown) remains unaltered on using either $n=3$ or $n=4$, *i.e.* a 2D or a 3D model. This drawback can easily be explained with the low density of the pellets which obviously impacts the measurements. Leaving out this argument, the 2D model obviously agrees better with the layered structure of VO₂ (B) (Fig. 1) and a favored conduction in the (ab) plan. Any deeper interpretation of the model constants should reasonably be discarded as they relate to the material and not to the compound itself; in particular, the metallic picture given above for the HT phase does not match with a variable range hopping-type mechanism. The difference curves between the data and the fits are actually more informative (insert in Fig. 6). They highlight some deviation to the mean behavior of the material (given by Mott's law) and reveal several anomalies with characteristic temperatures at i) 140 K for the initial departure from the mean behavior and ii) *ca* 205, 235 and 265 K matching the anomaly temperature

values reported above, which confirms the quality of VO₂ (B) pellets (the temperature for the anomaly at *ca* 205 K is actually 200 K upon cooling and 210 K upon heating). The Seebeck coefficient decreases with temperature and its magnitude, up to about 100 $\mu\text{V/K}$ at 150 K, is in agreement with the global semiconducting behavior of the material. The change of sign at 235 K during cooling and 237 K during heating indicates a change in the dominant charge carriers, from holes at LT to electrons at HT. The derivative curves show several regime changes with the characteristic temperature already mentioned at *ca* 140, 200, 235 and 265 K (here again, we note a small hysteresis for the change at *ca* 200 K). Although the Seebeck coefficient is believed to be less affected by the density of the material, the presence of a possible metallic regime at HT (only few tenth $\mu\text{V/K}$ with a linear domain *vs.* temperature) remains speculative and HT data on denser samples are needed to definitely conclude from such measurements.

The evolution of the capacitance with the temperature and frequency is shown in Fig. 7 for a cooling rate of 1 K/min. At 1 kHz, it is continuously decreasing from RT down to 203 K where it abruptly drops and finally continuously decreases down to 5 K; on heating with the same rate (not shown), it increases up to 211 K where it jumps (with the same magnitude than the drop during cooling) and then it again increases up to RT. The dielectric losses follow the same trend with drop/jump at the same temperatures but they are roughly constant at HT ($\text{tg}\delta \approx 200$) while they are continuously decreasing below the discontinuity to reach $\text{tg}\delta \approx 0.01$ at 5 K. Both the high capacitance and high dielectric losses at HT sign long range mobility while the lower capacitance and low dielectric losses at LT indicate the presence of localized carriers. The increase in the frequency makes the capacitance as well as the dielectric losses fall and progressively cancels the discontinuity, as shown in the first insert in Fig. 7; at *ca* 10 kHz, the discontinuity is no longer measurable. The second insert in Fig. 7 shows a log-log plot of the magnitude of the jump in the capacitance *vs* frequency; it highlights the strong effect of the frequency, a power law evolution but also a non-classical conduction mechanism. Indeed, in the case of a classical conduction mechanism, one should expect a $1/f$ dependence of the jump/drop at the transition; however, whatever the heating/cooling rate, the discontinuity scales here like $1/f^2$, suggesting a more complex mechanism. In addition, the hysteresis width strongly depends upon the temperature rate used on cycling the measurement: using a slow rate of ± 1 K/min, the width reaches 8 K while at ± 7 K/min, it reaches 81 K; in both cases the center of the hysteresis loop is at *ca* 207 K. Such broad evolution of the magnitude of the hysteresis width with the temperature rate indicates slow

dynamics of the mechanism implied in the transition and rules out an electronic-only process. Possible scenarios include, for instance, electron-lattice interactions or electron trapping on point defects. Taking into account the details of the structure and the behavior of the parent rutile polymorph, it is more likely to envisage the transfer of both electronic and elastic energies.

Fig. 8 shows normalized Nyquist diagrams as a function of temperature; the impedance modulus ranges from $10^2 \Omega$ at RT to $10^8 \Omega$ at 5 K and a normalization ($X_{Norm.}(f, T) = [X(f, T) - \min(X(T))]/[\max(X(T)) - \min(X(T))]$ where $X = Z'$ or Z'') was used to fit the full data range in a single plot and highlight the several regimes; full scales examples are displayed on the sides of the plot. At HT, the low frequency tail indicates extrinsic features and signs some delocalization of the carriers. On the other hand, the LT behavior below *ca* 237 K is typical of localized carriers. From *ca* 237 K down to 205 K, a small low frequency inductive loop is visible; although it is generally attributed to some adsorption process at the electrode surface, it could also be due to some stray capacitance artifact.²¹ The latter option is actually compatible both with the high impedance and low capacitance range in this temperature domain, and with the transition regime from a more delocalized HT state to a localized LT state. Below 205 K and down to about 140 K, most of the diagram can be modeled with a single RC arc.

As a summary of all this set of data, we note that the gradual change in electrical conductivity and thermal properties which occurs in the vicinity of 200K has a well define impact on magnetic and dielectric properties. This definitely links the electronic mobility to a transformation of the lattice spins and polarizability. Below, we discuss the possible mechanisms of these evolutions.

4. Discussion and conclusions

Though the MIT transition in VO₂ (B) might obey similar mechanisms than in the other polymorphs, the properties evolution is much smoother. The details of VO₂ (B) crystal structure are quite different and prevent from an abrupt change alike the one observed for the transition from VO₂ (M1) to VO₂ (R). In particular, unlike the case of VO₂ (M1) or even VO₂ (A) polymorphs, in which an obvious Peierls pairing can occur in the linear or zig-zag chains, the structure of the VO₂ (B) polymorph is more constrained and is unlikely to offer the

possibility of long range pairing although all the basic ingredients are present (d^1 state, “short” distances, AFM interactions). The shortest V2-V2 bond is separated by two (short and long) pairs and only a strong structural rearrangement would lead to a Peierls state. All the experimental results given above agree with the presence of several regimes below RT. Several properties could be modeled or explained assuming the coexistence over a wide range of temperature of a low, an intermediate and a HT phase. For the HT phase, transport measurements (Seebeck coefficient, AC data) as well as thermal (Debye temperature) and structural (short V-V distances) parameters strongly suggest a long range mobility associated to delocalized electrons (EPR, negative Seebeck coefficient) most probably spin polarized (Curie-like magnetization and magnitude of the magnetic field-dependent Sommerfeld coefficient which signs the presence of strongly correlated electrons²²); no direct proof of a strict metallicity ($\rho \propto T$) could be obtained because of the low density of the pellets; however, all results converge in this direction. This indicates that the HT phase of VO₂ (B) would follow closely the behavior of VO₂ (R); the structural data suggest an easy-plane (ab) conduction, although an easy conduction path along the zigzag chains cannot be fully discarded. According to Goodenough²³ the critical cation-cation separation below which an overlap of the neighboring cationic t_{2g} orbitals occurs and leads to itinerant electrons is 2.94 Å for vanadium oxides; if the nearest neighbor V–V distance along any particular direction is greater than 2.94 Å, one can expect d electrons to be localized at individual V ions, resulting in an insulating state; otherwise delocalization of the charge can lead to a metallic behavior. From DC transport measurements, the HT phase dominates down to *ca* 265 K; such critical temperature agrees both with the EPR data (the signal vanishes for $T > 280$ K) and the magnetization model (about 85% of HT phase at 265 K). In the IT region centered at about 235 K and extending roughly over 60 K, the magnetization data can be explained assuming the existence of an intermediate phase in which half of the spins are frozen. From the structural point of view, and as compared to the archetypal transition VO₂ (R) to VO₂ (M1), such a situation can easily be explained assuming that the close V2 cations pair off to form spin singlets. This picture is in agreement with the EPR results (breaking of the long range mobility and appearance of localized spins), the heat capacity data (drop in the Sommerfeld coefficient indicating the loss of correlations), Seebeck coefficient measurements (change of dominant carriers) and conductivity results (anomalies on AC and DC curves).

The LT phase appears at about 300 K and becomes dominant at about 200 K; however, from previous report and our results, it is never found alone. Within the models used

in this article, its maximum proportion is estimated between 69% and 75%. Note that the value of 69% used to model the magnetization data is the one reported by Oka⁷, and that a small deviation to this value is possible while keeping the overall quality of the model; such small tuning of p_{LT}^{max} only slightly impacts on the refined parameters and does not change the conclusions. The LT phase is marked with a strong localization (magnitude of transport properties, higher Debye temperature and zero Sommerfeld coefficient), a non-classical conduction mechanism ($1/f^2$ scaling of the discontinuity in AC transport measurements) and antiferromagnetic interactions (from EPR and magnetization data). It is worth noting that the system may undergo several other transitions at lower temperature. Indeed, resistivity curves, both AC and DC, display anomalies at about 140 K and the magnetization data clearly show an inflection of the curve at LT, likely marking a ferromagnetic ordering. The latter is compatible with the nature of the interactions of the LT phase (positive Curie-Weiss temperature) however, the origin of the anomaly at 140 K is unclear and could arise from either the low or HT phase (no trace of the intermediate phase is visible at this temperature).

Acknowledgments

The authors gratefully acknowledge the assistance of I. Bucur (INCEMC), A. Brull (ICMCB), S. Gomez (ICMCB), O. Nguyen (ICMCB) and S. Fourcade (ICMCB) during some of the characterizations. S.R.P., M.M., A.V., M.P. and A.A. gratefully acknowledge financial support from European Community's Marie Curie Initial Training Network (ITN) 7th Framework Programme - SOPRANO FP7/ 2007-2013 (Grant Agreement No. 214040) and European Community's Marie Curie Incoming International Fellowship (IIF) 7th Framework Programme - EPREXINA FP7/2007-2013 (Grant Agreement No. 255662) respectively.

Notes and references

¹ M. Schindler, F. C. Hawthorne and W. H. Baur, *Chem. Mater.* 2000, **12**, 1248.

² S. R. Popuri, M. Miclau, A. Artemenko, C. Labrugere, A. Villesuzanne and M Pollet, *Inorg. Chem.* 2013, **52**, 4780.

³ J. B. Goodenough, *J. Solid State Chem.*, 1971, **3**, 490.

⁴ M. Imada, A. Fujimori and Y. Tokura, *Rev. Mod. Phys.*, 1998, **70**, 1039-1263.

⁵ G. Seo, B-J. Kim, Y. W. Lee and H-T. Kim, *Appl. Phys. Lett.*, 2012, **100**, 011908.

⁶ M. Seo, J. Kyoung, H. Park, S. Koo, H. Kim, H. Bernien, B. J. Kim, J. H. Choe, Y. H. Ahn, H. T. Kim, N. Park, Q. H. Park, K. Ahn, and Dai-Sik Kim, *Nano Lett.* 2010, **10**, 2064.

-
- ⁷ Y. Oka, T. Yao, N. Yamamoto, Y. Ueda and A. Hayashi, *J. Solid State Chem.*, 1993, **105**, 271.
- ⁸ S. A. Corr, M. Grossman, Y. Shi, K. R. Heier, G. D. Stucky and R. Seshadri, *J. Mater. Chem.*, 2009, **19**, 4362.
- ⁹ W. Li, J. R. Dahn and D. S. Wainwright, *Science*, 1994, **264**, 1115.
- ¹⁰ J. Liu, Q. Li, T. Wang, D. Yu and Y. Li, *Angew. Chem. Int. Ed.*, 2004, **43**, 5048.
- ¹¹ G. S. Zakharova, I. Hellmann, V. L. Volkov, C. Täschner, A. Bachmatiuk, A. Leonhardt, R. Klingele and B. Büchner, *Mater. Res. Bull.* 2010, **45**, 1118.
- ¹² J. Liu, Q. Li, T. Wang, D. Yu and Y. Li, *Angew. Chem. Int. Ed.*, 2004, **43**, 5048.
- ¹³ F. Theobald, R. Cabala and J. Bernard, *J. Solid State Chem.* 1976, **438**, 431.
- ¹⁴ J. Rodríguez-Carvajal, *Physica B*, 1993, **192**, 55.
- ¹⁵ P. Dordor, E. Marquestaut and G. Villeneuve, *Rev. Phys. Appl.*, 1980, **15**, 1607; P. Dordor, E. Marquestaut, C. Salducci and P. Hagenmuller, *Rev. Phys. Appl.*, 1985, **20**, 795.
- ¹⁶ R. A. Theerthan, A. Artemenko and M. Maglione, *J. Phys.: Condens. Matter*, 2012, **24**, 405901.
- ¹⁷ S. R. Popuri, M. Miclau, A. Artemenko, C. Labrugere, A. Villesuzanne and M. Pollet, *J. Solid State Chem.*, 2014, **213**, 79.
- ¹⁸ J. P. Pouget, H. Launois, T. M. Rice, P. Dernier, A. Gossard, G. Villeneuve and P. Hagenmuller, *Phys. Rev. B*, 1974, **10**, 1801.
- ¹⁹ D. B. McWhan, M. Marezio, J. P. Remeika and P. D. Dernier, *Phys. Rev. B*, 1974, **10**, 490.
- ²⁰ N. F. Mott, *Phil. Mag.*, 1969, **19**, 835.
- ²¹ J. Fleig, J. Jamnik, J. Maier and J. Ludvig, *J. Electrochem. Soc.*, 1996, **143**, 3636.
- ²² M. Pollet, M. Blangero, J. P. Doumerc, R. Decourt, D. Carlier, C. Denage and C. Delmas, *Inorg. Chem.*, 2009, **48**, 967.
- ²³ J. B. Goodenough, *Annual Review of Materials Science*, 1971, **1**, 101.

Table 1: Parameters adjusted to fit the magnetization data. C : Curie constant with into brackets the percentage of a half spin; θ : Curie-Weiss temperature; χ_0 : temperature independent term.

| | C (% $S_{1/2}$) | θ (K) | χ_0 (emu/mole) |
|-----------------|--------------------|--------------|---------------------|
| LT phase | 0.045 (12%) | 11.3 | 213.10^{-6} |
| IT phase | 0.1875 (50%) | - | - |
| HT phase | 0.375 (100%) | -308 | -47.10^{-6} |

Table 2: parameters used to fit the heat capacity data recorded at 0 T and 9 T; Debye 1&2 with N: number of oscillators; θ_D : Debye temperature; γ : Sommerfeld coefficient; Δ : Energy term and its proportion 'n' for the Schottky contribution.

| Magnetic Field | Debye 1 | | Debye 2 | | γ (mJ/mol.K ²) | Schottky | |
|---------------------------|----------------|----------------|----------------|----------------|--------------------------------------|-----------------|-------|
| | N | θ_D (K) | N | θ_D (K) | | Δ (K) | n |
| 0 T | 0.79 | 335 | 2.21 | 850 | 7.15 | 10/27 | 0.027 |
| 9 T | 0.73 | 314 | 2.27 | 851 | 19.2 | 15 | 0.024 |

Figure 1. 3D sketch of VO_2 (B) crystal structure at 300 K. Vanadium ions are shown as orange (V1) and brown (V2) spheres; small red spheres represent oxygen ions. V-V bond lengths are also given for the several possible close pairs and are identified with different colors.

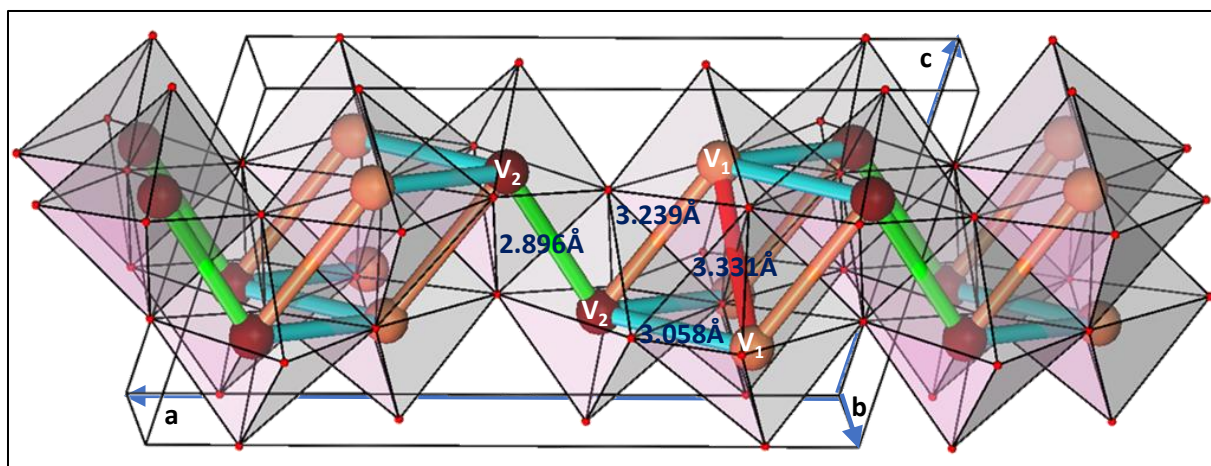


Figure 2. (a) XRPD patterns of as synthesized VO_2 (B) platelets, on the surface of SPS treated pellets and as synthesized VO_2 (M1). SEM overview morphology images of (b) as-synthesized VO_2 (B) plate-like crystals prepared using hydrothermal process at 493 K for 2 hr (as described in the text) and (c) cross-sectional overview of a pellet obtained by SPS under 523 K - 90 MPa conditions.

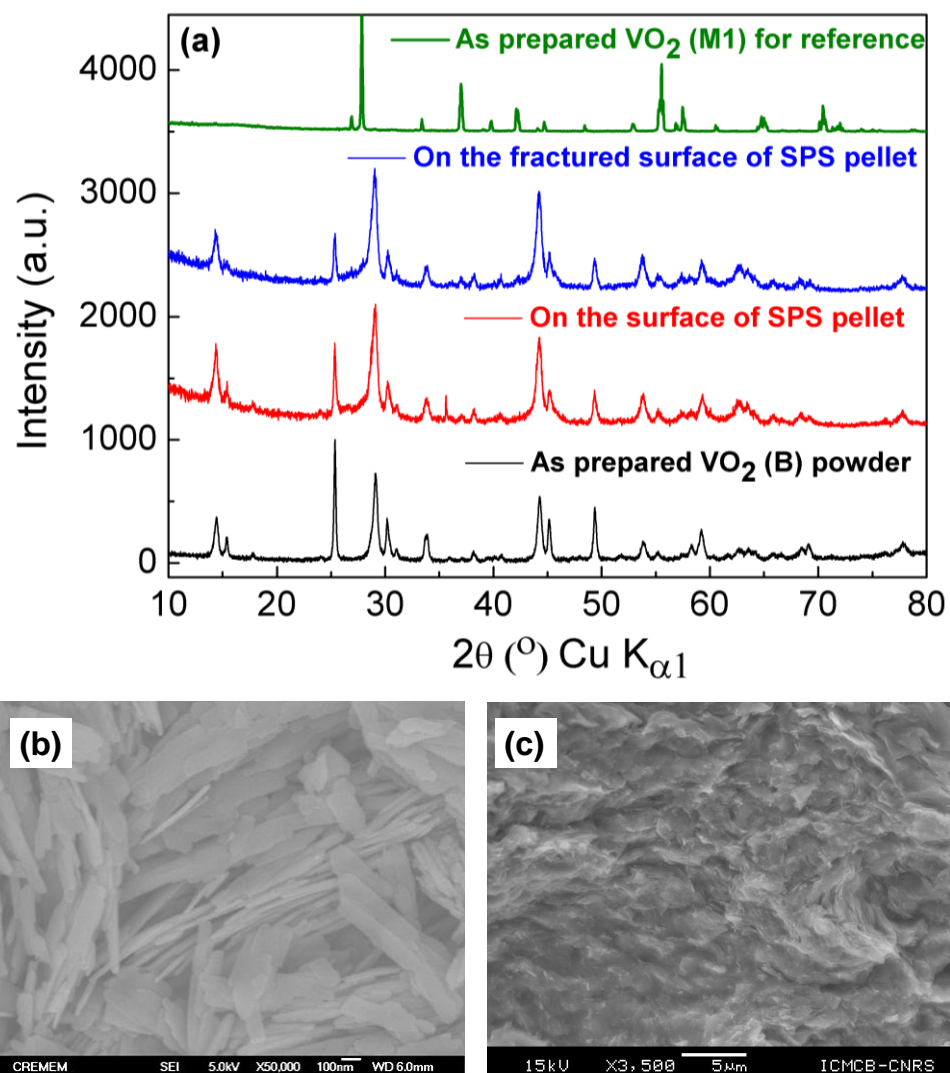


Figure 3. Temperature dependence of the magnetic susceptibility in zero field-cooled (ZFC, circles) and field-cooled (FC, triangles) regimes recorded in DC field $H=1000$ Oe. The bottom panel is a plot of the phase proportion used in the fit: the blue dashedline represents the LT phase proportion following the results of Oka et al. (Ref. 7, black circles); the green dottedline represents the proportion of an intermediate temperature region phase (zeroed if not used); the red line represents the high temperature phase proportion. The fits to the magnetization include either the low and high temperature phases only (green dashed line) or the low and high temperature phases plus an intermediate regime as discussed in the text (red line). The top right insert ($\propto 1/M$) zooms in the intermediate temperature region.

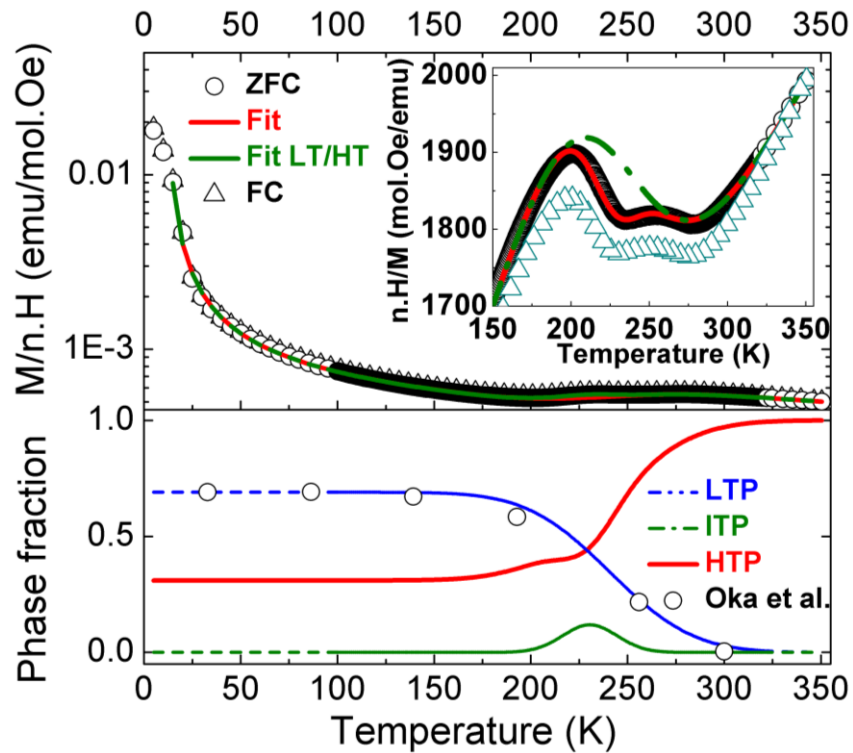


Figure 4. Experimental X-band EPR spectra of VO₂ (B) recorded from 180 K to RT. Colors (red at 300 K; green from 280 to 240 K; blue below 230 K) indicates the several regimes discussed in the text.

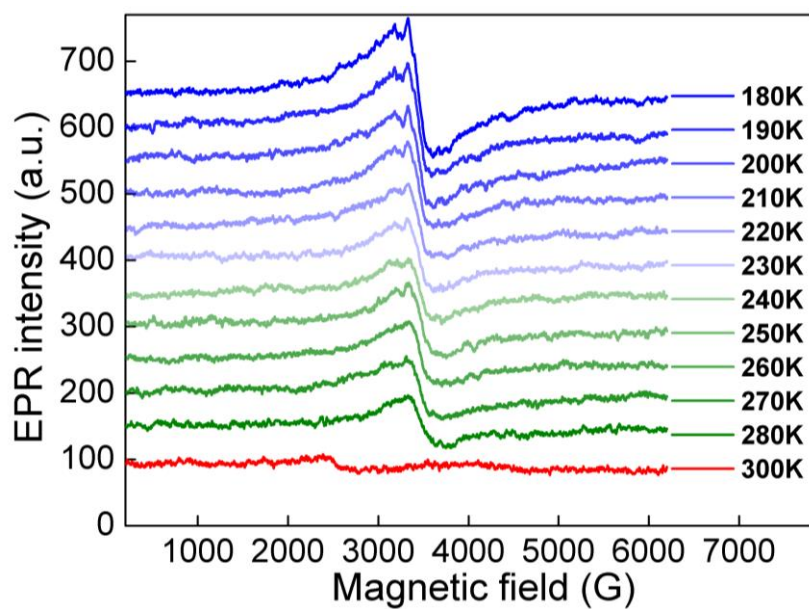


Figure 5. Specific heat data for VO_2 (B), measured without magnetic field (blue circles) and under a 9 T magnetic field (red squares). The grey dashed line is the difference in heat capacity with and without applied magnetic field; the green dashed lines are guide for the eyes highlighting the different regimes at low and high temperature; the vertical green dotted lines mark some anomalies in the difference curve at *ca* 200 K and 233 K. The insert zooms in the LT region.

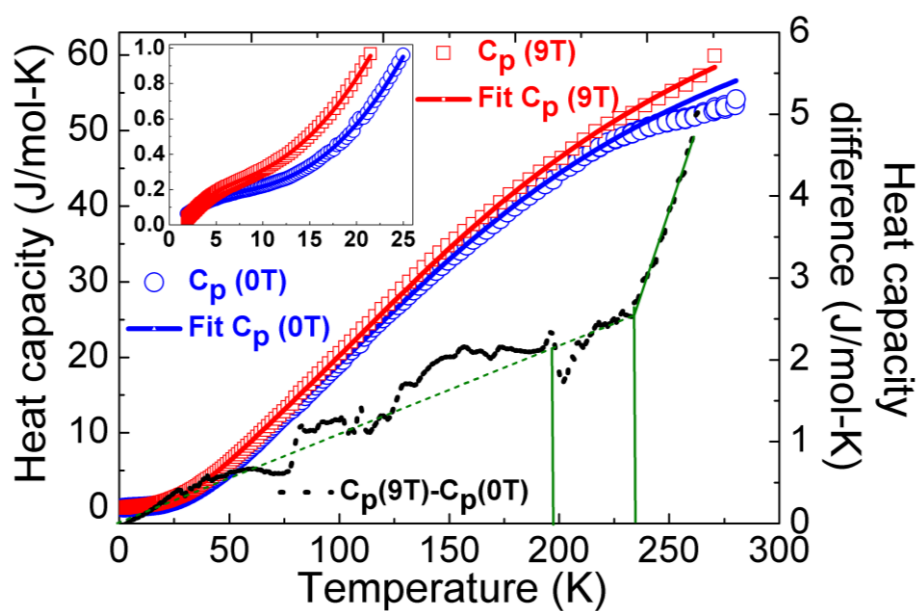
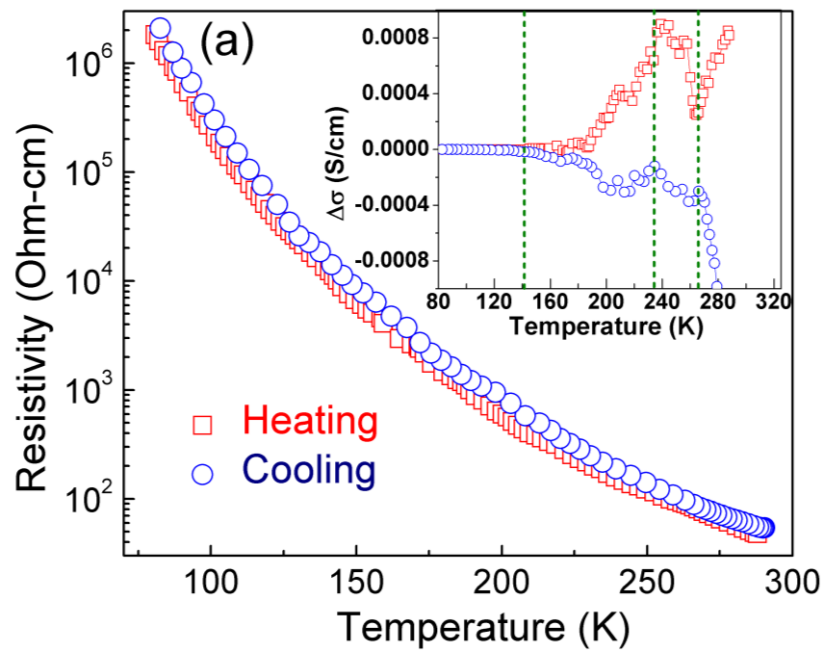


Figure 6. Temperature dependence of the DC transport properties of VO₂ (B). (a) Electrical resistivity (insert: deviation to 2D variable range hopping model); (b) Seebeck coefficient (open symbols) and its temperature derivative (dashed and dotted lines). In both cases, the (green) vertical dashed and shaded lines mark characteristic temperatures with anomalies or departure from the mean behavior.



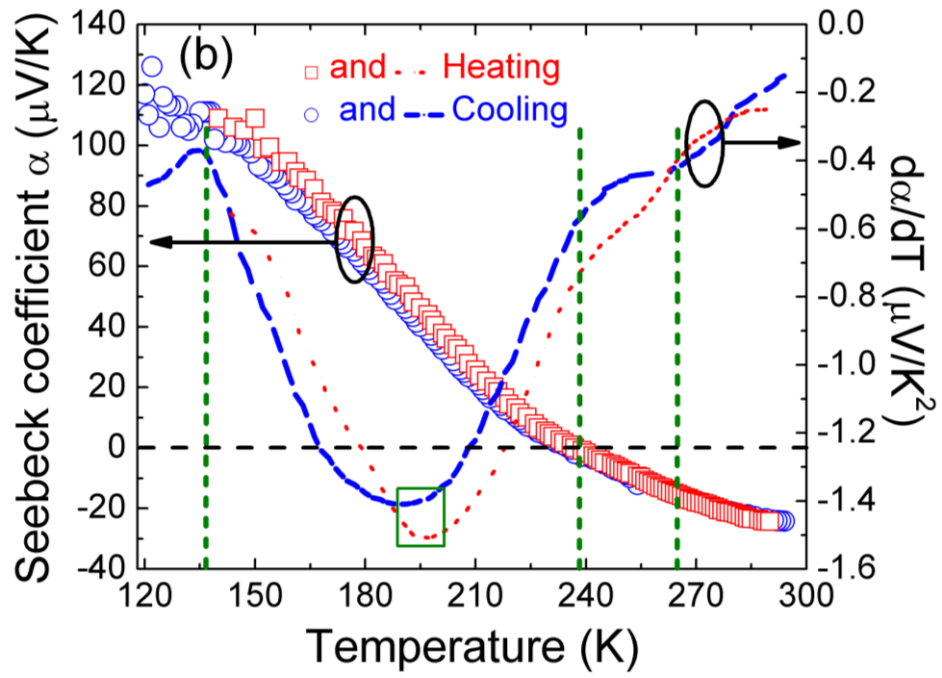


Figure 7: Temperature and frequency (log scale) dependence of the capacity (log scale); the first insert zooms in the main plot and highlights the jump in the capacity as T crosses ca 207 K; the second insert plots the magnitude of the jump (log scale) as a function of the frequency (log scale) for several rates (± 1 and ± 7 K/min) as well as a full lines with slope = -2.

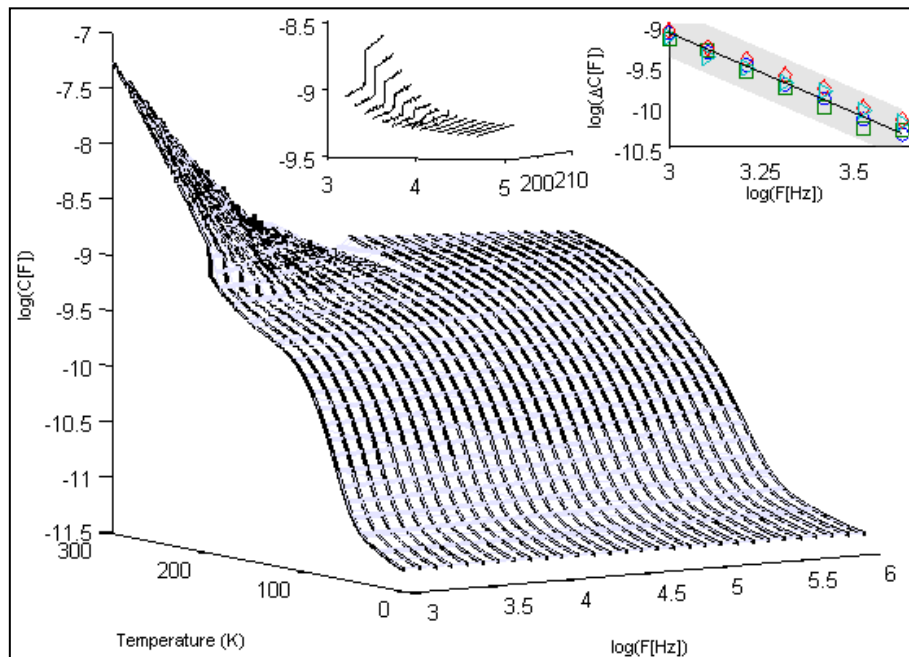


Figure 8. Normalized impedance plots ($Z''(\text{freq.})$ vs $Z'(\text{freq.})$) as a function of temperature; the normalization is used to fit the full data range (eight orders of magnitude in Z) in a single plot and highlights the several regimes; full scale examples (all data in Ω) are shown on the bottom and right sides for different temperatures; arrows in these inserts point to magnified plots of the circled areas.

